

Characterizing microearthquakes and shallow structure with dense array and optical fibers

by

Hilary Chang

Submitted to the Department of Earth, Atmospheric, and Planetary Sciences
in partial fulfillment of the requirements for the degree of

DOCTOR OF PHILOSOPHY

at the

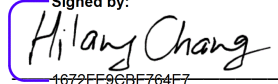
MASSACHUSETTS INSTITUTE OF TECHNOLOGY

May 2025

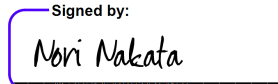
© 2025 Hilary Chang. All rights reserved.

The author hereby grants to MIT a nonexclusive, worldwide, irrevocable, royalty-free license to exercise any and all rights under copyright, including to reproduce, preserve, distribute and publicly display copies of the thesis, or release the thesis under an open-access license.

Authored by: Hilary Chang
Department of Earth, Atmospheric, and Planetary Sciences
May 1, 2025

Signed by:

1672FE0CBE764E7...

Certified by: Nori Nakata
Principal Research Scientist, Thesis Supervisor

Signed by:

AD691A4295A348C...

Accepted by: W. David McGee
Department Head, and
William R. Kenan, Jr. Professor of Earth and Planetary Sciences
Department of Earth, Atmospheric, and Planetary Sciences

Signed by:

6D00717B522F4DD...

Chapter 6

Characterizing microearthquake source parameters and attenuation using downhole DAS array at the Cape Modern geothermal field

Summary: Distributed Acoustic Sensing (DAS) is a great tool for microearthquakes ($M < 2$) and structure characterization. For downhole cables, the densely distributed receiver channels can resolve along-depth attenuation. The cable that is closer to the source captures high-frequency signals that are crucial for estimating the source properties of the small earthquake. We propose a workflow for estimating source parameters using the downhole DAS cable at the Cape Modern geothermal field. The microearthquakes occurred during stimulation in 2024. We first resolve the DAS instrument response using the apparent velocity of the target P waves and channel separation. Then, we estimate the attenuation using an along-depth deconvolution method. Finally, we characterize the stress drop, source dimension, and magnitudes using single spectra and spectral ratio methods. We can characterize events between moment magnitude -0.5 – 1.7. The majority of stress drops are between 1 and 10 MPa and generally follow a constant trend among magnitudes. We observe an increasing stress drop with increasing distance from the injection, which agrees with previous studies. The downhole cable allows us to characterize small events that are important for understanding how the subsurface responds to injections.

6.1 Introduction

During operations in a geothermal reservoir, microearthquakes help us understand the response of the subsurface. In an enhanced geothermal reservoir where rocks are being stimulated to increase the permeability, microearthquakes provide information on the extent

of fractures. The source properties such as stress drop, corner frequency, and magnitudes are related to the size of ruptures and the energy released. This information helps us optimize the stimulation efficiency and prevent triggering larger earthquakes. The events usually have small magnitudes (e.g., $M < 2$). To characterize their source properties, we need borehole sensors to capture the high-frequency energy (e.g., > 100 Hz).

However, borehole geophones are expensive to deploy. Also, mechanical sensors do not like the high temperature and high pressure in the downhole environment. A useful tool that overcomes these difficulties is Distributed Acoustic Sensing (DAS). DAS turns fiber-optic cables into densely distributed vibration sensors ([Zhan, 2020](#)). The cable can endure harsh downhole environments and become a dense seismic network in the subsurface. Deployed cables can be repeatedly used for long-term monitoring.

To use DAS in conventional seismic analysis methods, we need to account for the instrument response. DAS measures strain or strain rate using a gauge length, which is usually several meters. The gauge length puts a kernel on the spectra and can mute signals of certain wavelengths ([Bakku, 2015](#); [Hartog, 2017](#)). These affect earthquake source characterization using single event spectra, which relies on the spectral amplitude. Here, we estimate the instrument response and correct the earthquake spectra.

Some studies dealt with the DAS instrument responses using spectral ratio approach (e.g., [Chen, 2023](#); [Lior, 2024](#)). The spectral ratio approach cancels common path and site terms and instrument responses using collocated events as the Empirical Green's Function (EGF) (e.g., [Hartzell, 1978](#); [Hough, 1997](#)). However, the EGF brings in other uncertainties ([Abercrombie, 2015](#)). Here, we cross-validate source characterization using both single spectra and the spectral ratio approaches, which help us examine the assumptions and uncertainties behind them.

The goal of the research is to develop a workflow for downhole source parameter estimation using DAS. In the following, we first introduce the data and the site. We use the microearthquake catalog from one week of stimulation in the Cape Modern geothermal field in Utah. Then, we investigate the instrument response and unit conversion for DAS strain/strain rate data. After that, we perform attenuation analysis, followed by source parameter estimation using single spectra and spectral ratio approaches.

6.2 Data

Figure 6.1 shows the microearthquakes and wells during one week at the Cape Modern geothermal field ([Nakata et al., 2024](#)). The week was in the middle of months of stimulation for enhancing subsurface permeability. There are more than 7000 microearthquake events in the catalog detected by DAS, surface nodal geophones, and regional networks. We focus on the data recorded by the cable in the vertical well 1OB. We choose 1155 events (locations shown in Figure 6.1). These events have reliable arrival picks using an automatic picker and visual inspection.

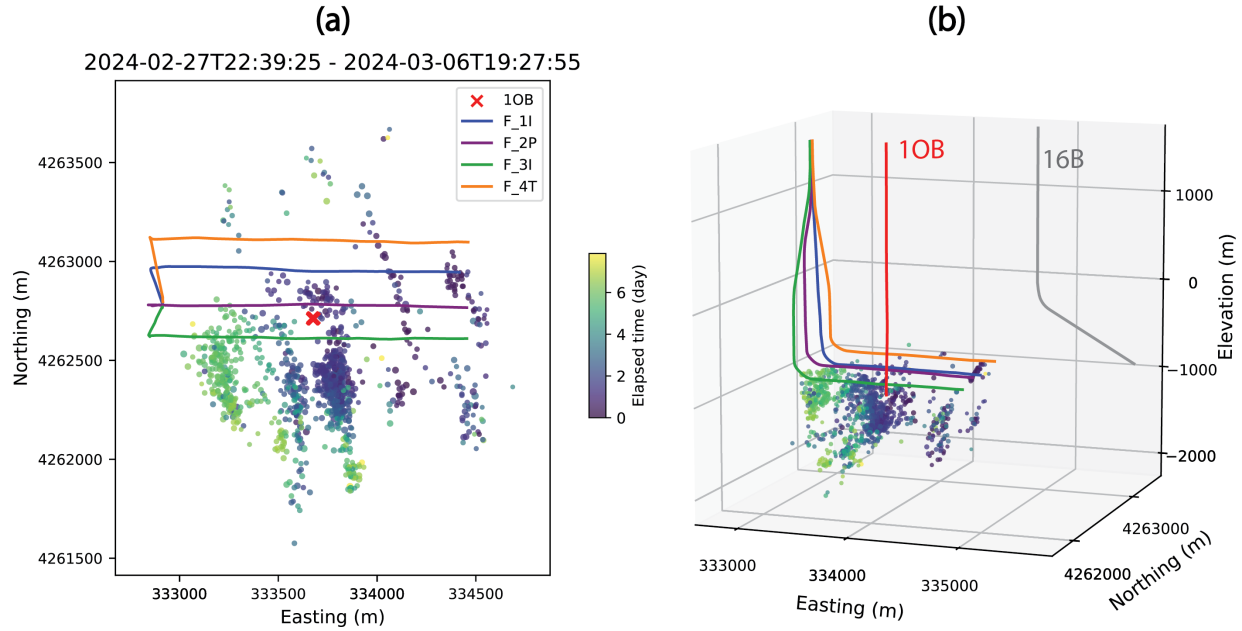


Figure 6.1: Events during a week of stimulation (2024-02-27 – 2024-03-06) on the (a) 2D and (b) 3D maps at the Cape Modern geothermal field. The curves are the trajectories of the wells. Wells F-2P and F-3I were actively injected during the occurrence of these earthquake events. We focus on the Distributed Acoustic Sensing (DAS) data along the fiber-optic cable in the vertical well 1OB in this study. Well 16B is another observation well in Utah Forge.

We use the catalog event origin times and location coordinates, which are determined using a double-difference algorithm in a 3D velocity model ([Nakata et al., 2025](#)). The catalog contains moment magnitude (M_w) estimates based on the maximum amplitude recorded by the surface arrays and an empirical relation. The catalog M_w is between 0.5 and 1.9; however, the quality of these M_w estimates is uncertain.

The downhole DAS system (Silixa iDAS) in the vertical well 1OB has 1600 channels. The channel separation is approximately 2 m. The sampling rate is 1000 Hz. The unit of the raw data is proportional to the strain rate. Figure 6.2 shows a M_w (catalog) 1.74 event recorded by the DAS cable. The arrivals of different phases are well captured by the cable in the deep borehole.

Figure 6.3 shows the Fourier spectra of the P waves (calculated from Figure 6.2b). The P-wave spectra are above the noise level from 20 Hz to more than 200 Hz. The deeper channels (> channel 800) have a signal above noise up to the Nyquist frequency of 500 Hz. The signals of shallower channels experience larger spectral decays on the higher-frequency side, which can be attributed to the instrument response and the attenuation. In the following sections, we introduce the DAS instrument response and analyze the influence of different factors.

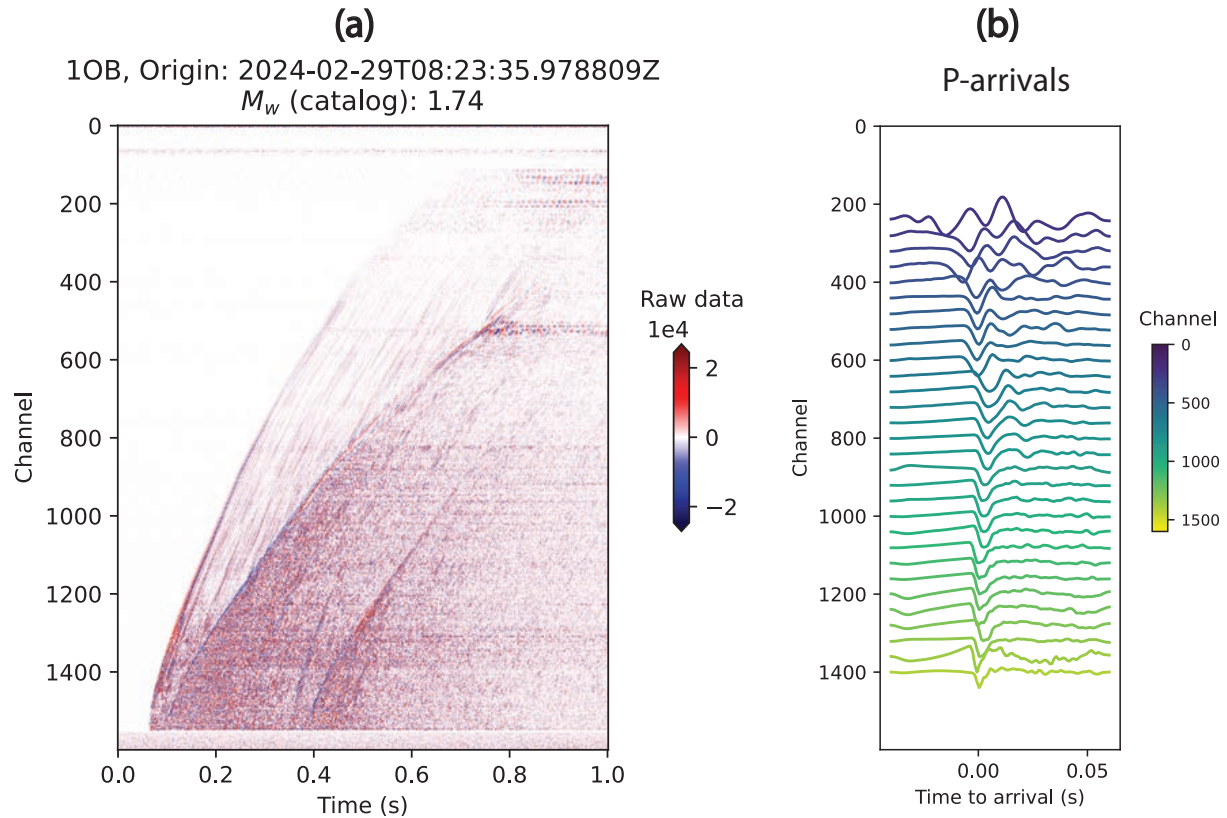


Figure 6.2: A microearthquake event (catalog $M_w = 1.74$) during stimulation. **(a)** The arrival wavefield is captured by the optical fiber along the vertical well 1OB. The raw data amplitude is proportional to the strain rate. **(b)** Raw P-wave arrivals (-0.04 – 0.06 s relative to P-arrival times). The arrivals are picked by an automatic kurtosis picker. The waveforms in **(b)** are normalized by the maximum amplitude.

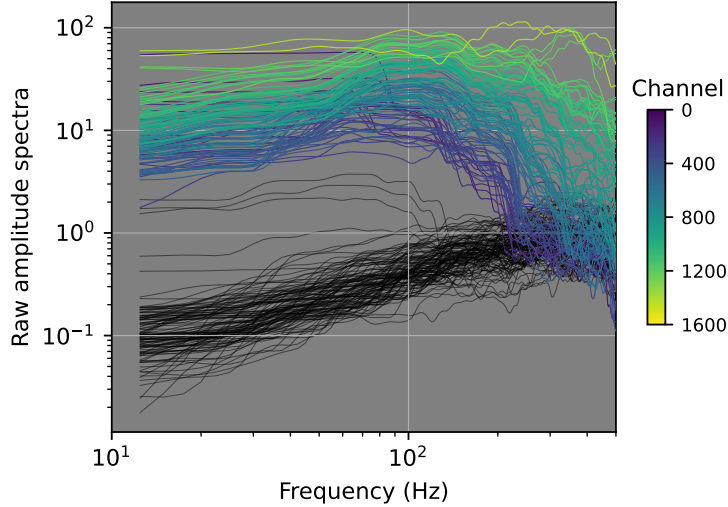


Figure 6.3: Raw P-wave spectra (color curves) from deep (yellow) to shallow (blue) channels for the M_w 1.74 event in Figure 6.2. The spectra are calculated in a time window of -0.04 – 0.06 s relative to the P-arrival. The black curves are the noise spectra (0.3 s before the P-arrival).

6.3 Instrument response and unit conversion for DAS

6.3.1 The gauge length effect

The DAS uses a gauge length to measure strain. The finite length distorts the spectra. The gauge length response ($\frac{\dot{\varepsilon}_{DAS}}{\dot{\varepsilon}}$) can be calculated by (Bakku, 2015; Hartog, 2017):

$$\frac{\dot{\varepsilon}_{DAS}}{\dot{\varepsilon}} = \text{sinc}\left(\frac{L}{\lambda_{app}}\pi\right), \quad (6.1)$$

$$= \text{sinc}\left(\frac{fL}{c\pi}\right), \quad (6.2)$$

in which L is the gauge length, λ_{app} is the apparent wavelength, f is frequency, and c is the apparent phase velocity. Note that $\frac{\dot{\varepsilon}_{DAS}}{\dot{\varepsilon}} = 0$ when L is an integer multiple of λ_{app} .

Figure 6.4 shows the response for a gauge length of 10 m. Waves with a larger apparent wavelength are less susceptible to the gauge length response. As the wavelength gets smaller and closer to the gauge length, the amplitude distortion increases (Figure 6.4a). The response is 0 when $\lambda_{app} = 10$ m, 5 m, $\frac{10}{3}$ m, Converting the response to the frequency domain ($f = c/\lambda_{app}$) using an apparent phase velocity $c = 3$ km/s, we get a notch in the response spectra at 300 Hz (Figure 6.4b). For the same wave (same λ_{app}), a medium with a slower velocity makes the response hit the notch at a lower frequency, and therefore, is more susceptible to gauge length distortion.

We can observe the gauge length effect in the frequency-wavenumber domain (Figure 6.5). For a gauge length of 10 m, the amplitudes are suppressed as they approach a wavenumber

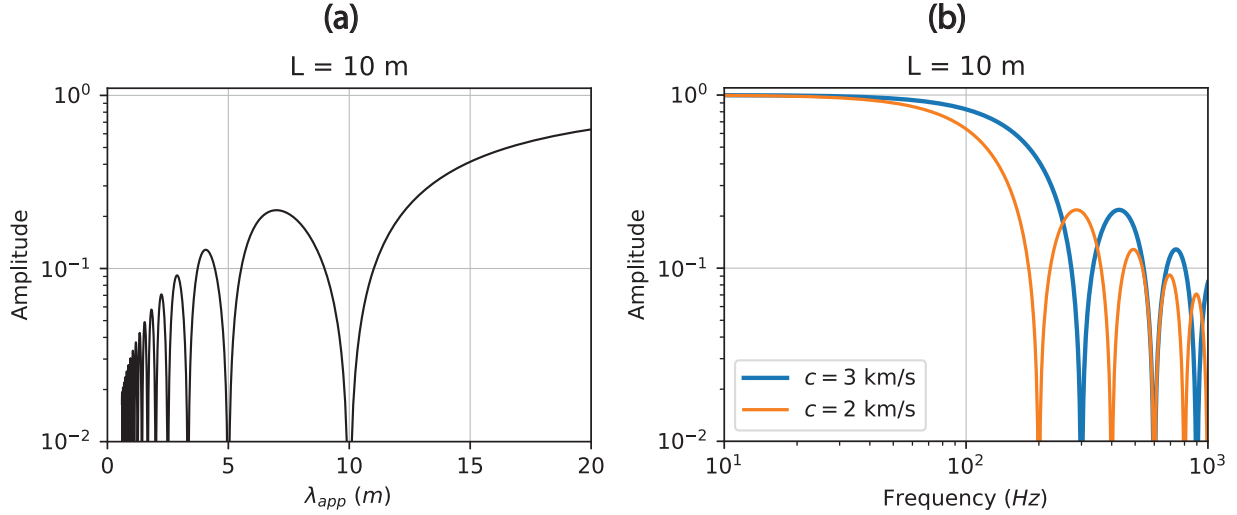


Figure 6.4: The gauge length response for a gauge length $L = 10$ m. (a) In the apparent wavelength (λ_{app}) domain. (b) In the frequency (f) domain. The blue and yellow curves represent the same waves (same λ_{app}) with different medium velocities. A medium with a slower velocity is more susceptible to spectral distortion.

of 0.1 m^{-1} . Waves with slower apparent velocity (the S waves with a steeper slope in Figure 6.5b) are more affected by the gauge length distortion.

6.3.2 Unit conversion

The raw DAS data collected by Silixa iDAS is proportional to the strain rate. To convert the data to displacement, we use the following equations.

The unit of the raw data is radians per second (s) per gauge length L . Converting the raw data to strain rate ($\frac{\partial \varepsilon}{\partial t}$) involves a scalar:

$$\frac{\partial \varepsilon}{\partial t} = \frac{\text{radian}}{s \cdot L} \cdot G. \quad (6.3)$$

The unit of $\frac{\partial \varepsilon}{\partial t}$ is nanometers (nm) per meter (m) per second. L is 10 m. G is the conversion factor provided by the interrogator provider (Silixa):

$$G = 116.0 \cdot 2 \times 10^{-13} \cdot fst/L \quad (6.4)$$

The conversion factor is related to data compression and the relationship between optical phase shift and strain. fst is the sampling rate (1000 Hz).

For plane-wave incidence, strain is proportional to the particle velocity (Bakku, 2015; Wang et al., 2018):

$$\dot{u} = c\varepsilon, \quad (6.5)$$

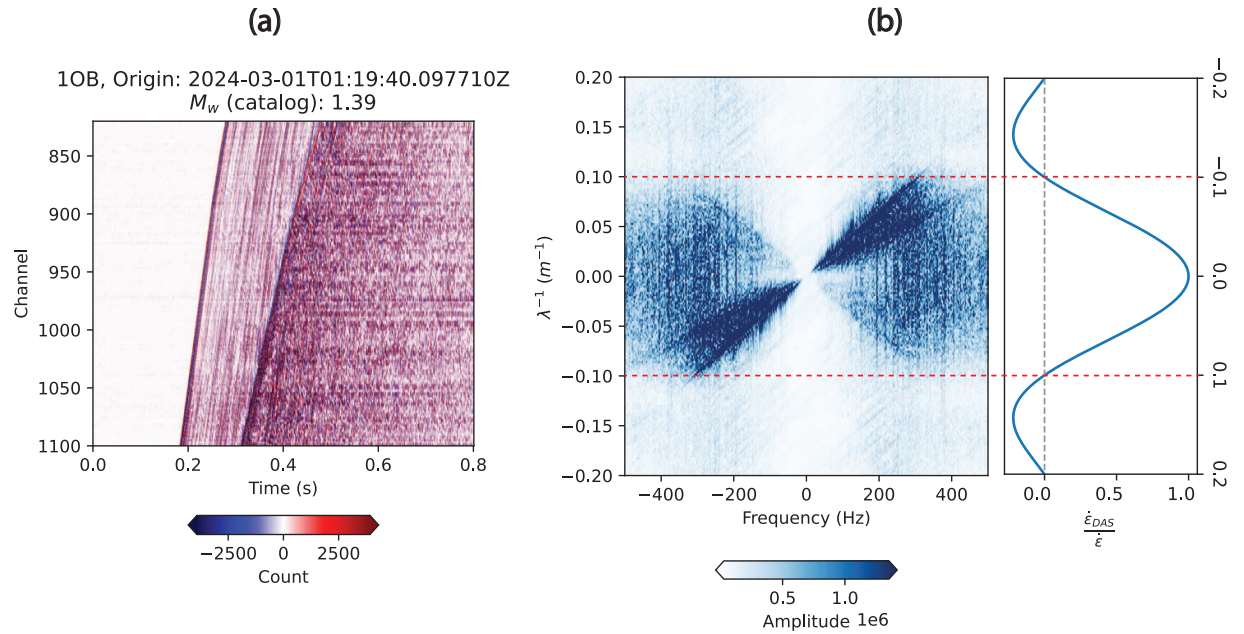


Figure 6.5: The body-wave wavefield for an event (catalog $M_w = 1.39$) (a) in the time-space domain and (b) in the frequency-wavenumber domain. $\frac{\dot{\epsilon}_{DAS}}{\dot{\epsilon}}$ is the gauge length response for a gauge length $L = 10 \text{ m}$. The first amplitude notch is at the absolute wavenumber ($|\lambda^{-1}|$) = 0.1 m^{-1} (horizontal dashed lines in red). Waves with slower apparent velocity (having a steeper slope in [b]) are more susceptible to the notch.

in which c is the apparent phase velocity. Hence, we can convert strain rate (proportional to acceleration) to particle displacement (u) by integrating strain rate twice in time and multiplying the apparent velocity:

$$u(t) = \left(\sum_{t=0}^{N_t} \sum_{t=0}^{N_t} \frac{\partial \varepsilon}{\partial t} \right) \cdot \frac{c}{fst^2} \cdot \frac{1 \text{ m}}{10^9 \text{ nm}}. \quad (6.6)$$

The unit of $u(t)$ is meter. N_t is the number of time samples. Equation 6.6 assumes plane waves across the gauge length. Note that Equations 6.3 – 6.5 only change the amplitude (not phase), hence, are only needed if such information is relevant (e.g., magnitude estimation).

To summarize, for plane waves, we can use the apparent velocity to calculate both the unit conversion factor and the gauge length response. If only phase information is needed (e.g., travel time analysis) or if an EGF is available for canceling out the instrument response, we can use raw strain or strain rate data. However, we still need to be aware of losing signals for waves with apparent wavelengths that are close to the gauge length. If we want to measure relative spectral shape (e.g., spectral attenuation, the corner frequency of the source spectrum), we need to correct for the gauge length effect (Equation 6.2). If the absolute amplitude is needed (e.g., magnitude estimation), we have to correct the gauge length effect and convert the unit to particle motions (Equations 6.2 – 6.6).

6.4 Attenuation analysis

Method

We select the 25 largest events located at the bottom of well 1OB for the attenuation analysis. The events are at least 0.4 km below the lowest channel and within a 0.4 km radius from the well. The location requirements ensure that we characterize mostly attenuation in the vertical direction. We window the raw P waves at -0.1 – 0.15 s around the P arrivals picked by a Kurtosis picker (Beyreuther et al., 2010). We demean, detrend, taper both ends of the trace, and calculate the Fourier spectra using a multitaper method (Prieto, 2022). Figure 6.6a shows the P wave spectra of an event. The spectral decay on the high-frequency spectra can be associated with attenuation and the gauge length effect.

We need to remove the velocity-dependent gauge length response that alters the shape of the spectra. We calculate the gauge length response for each channel based on the apparent velocity estimated by P-arrivals and the actual separation of the channels (Figure 6.6b). We set a high-frequency cutoff amplitude at a water level of 0.4 for the response spectra to prevent amplifying noise, and we discard channels with cutoff frequency < 200 Hz. Then, we remove the response by dividing the raw spectra by the response spectra (Figure 6.6c). We do not need to convert the unit to particle motions because we only consider the relative spectral decay later in the analysis. We stack spectra for neighboring channels within 20 m to enhance the signal-to-noise ratio (SNR).

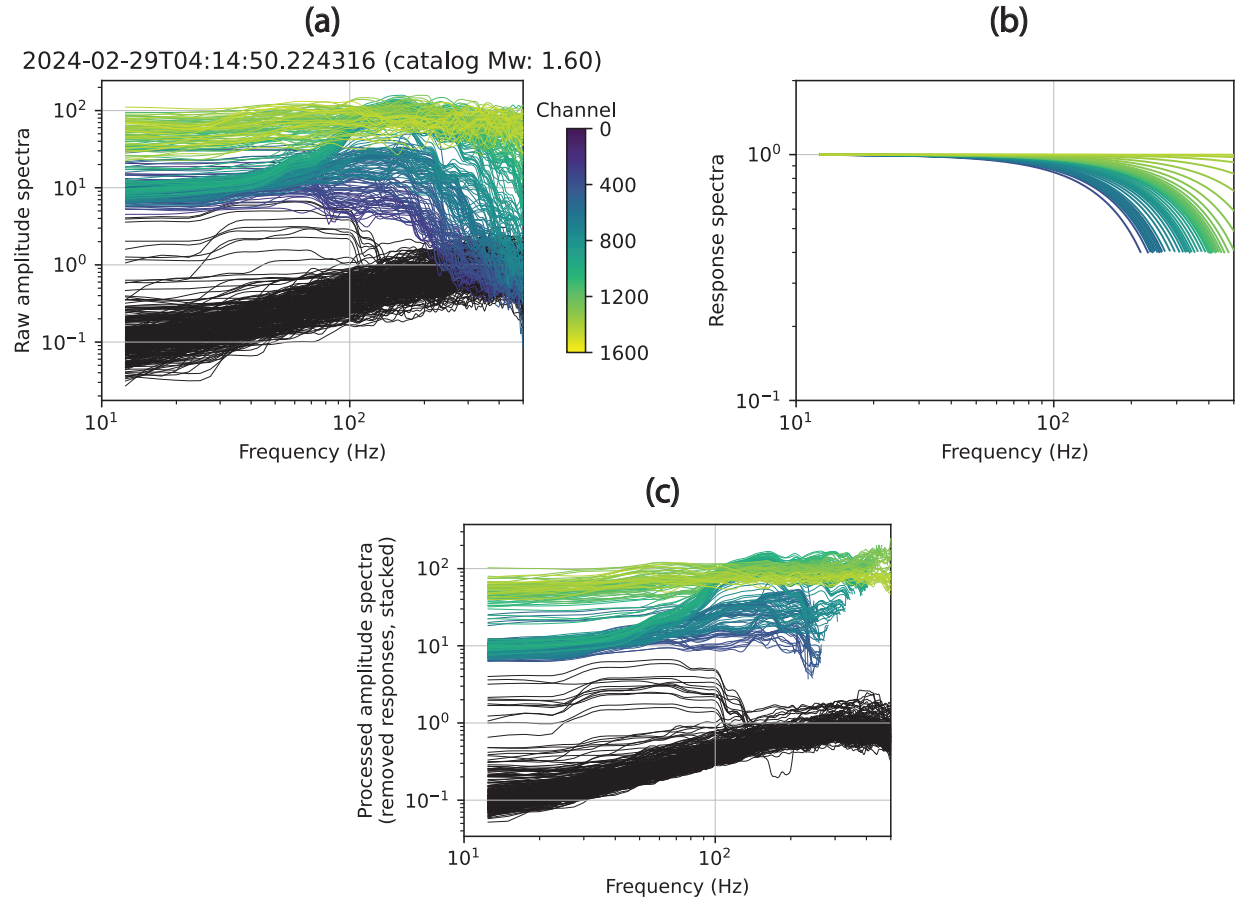


Figure 6.6: Removing the channel-dependent gauge length response for an example event. **(a)** The raw P-wave spectra (windowed at -0.1 – 0.15 s relative to the picked P arrival). We plot only 1/5 of the spectra for clearer visualization. Signal spectra are colored by channel numbers. Noise spectra are in black. **(b)** Response spectra are calculated based on apparent velocities estimated by P-arrivals and actual channel separations. We set a high-frequency cutoff at a water level of 0.4 to prevent amplifying noises. Channels with a cutoff frequency < 200 Hz are discarded. **(c)** Processed amplitude spectra after dividing the raw spectra in **(a)** by the response spectra in **(b)** and then stacking channels within a 20 m distance.

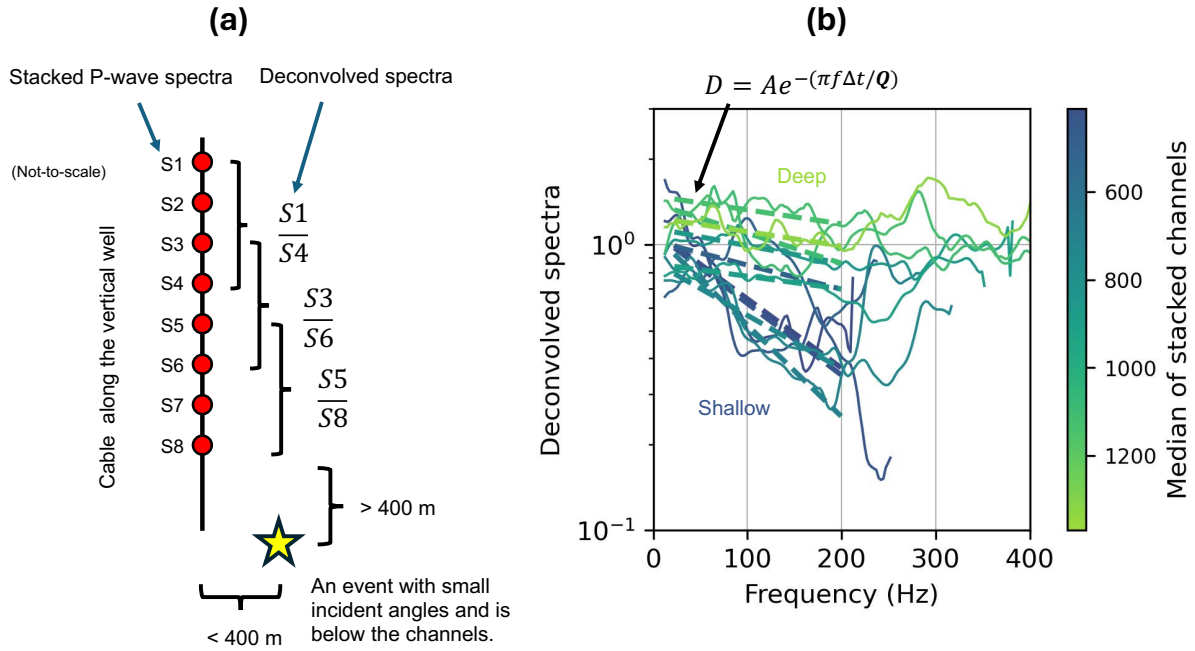


Figure 6.7: (a) A schematic illustration of the deconvolution for the attenuation analysis (not to scale). For an event at the bottom of the cable (with a 0.4 km distance), we first stack the P-arrival spectra every 20 m (10 channels). Then, we deconvolve the stacked spectra by another stacked spectra 160 m (80 channels) below. (b) The deconvolved spectra. We fit the spectra with an exponential function (D) between 20 and 200 Hz (limited by the gauge length) to estimate the Q values. Note that shallower channels (darker colors) have a more rapid spectral decay due to higher attenuation (lower Q).

Then, we perform along-depth deconvolutions in which we divide the stacked spectra by another stack that is 80 channels (~ 160 m) below (Figure 6.7a). The deconvolution removes the source term, and the deconvolved spectra represent the wave propagation effects along the wellbore (Figure 6.7b). The deconvolved spectra at shallower depths tend to experience a higher spectral decay between 20 – 200 Hz because of a higher attenuation.

We estimate the Quality Factor (Q) by fitting the deconvolved spectra (D) between 20 and 200 Hz with (Anderson & Hough, 1984)

$$D = Ae^{-\pi f \Delta t / Q}, \quad (6.7)$$

where A is an arbitrary low-frequency amplitude, Δt is the travel time difference between the deconvolved channels, and Q is the Quality Factor.

Results

Figure 6.8a shows the Q values along the vertical well 1OB. In the sediment column (surface to around 1.5 km depth), Q generally increases with depth. The top 0.5 km has a much lower Q ($Q = 20 - 60$) than the sediments below ($Q = 50 - 200$). The transition between

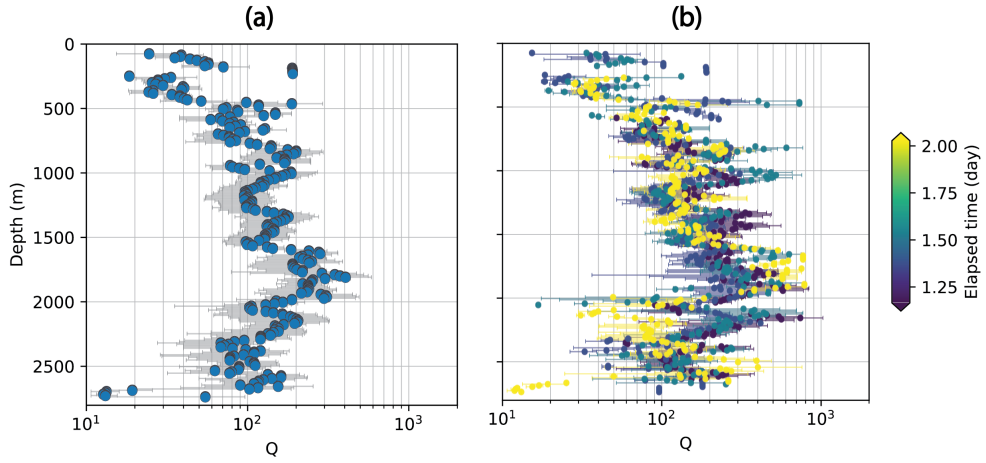


Figure 6.8: Quality factor (Q) profiles estimated by deconvolved P-wave spectra of 25 microearthquake events (catalog $M_w = 1.4 - 1.7$). The selected events are located near the bottom of well 1OB (within a 0.4 km horizontal distance and at least 0.4 km lower than the last measurement point). Each dot is the median Q estimate of the closest 10 channels. The error bars are standard deviations. (a) All Q estimates. (b) Q estimates from events at different times of the day.

sediment and granite is likely between 1.5 – 2.0 km, with the highest Q at 200 – 600. Below 2.0 km, most Q values are between 50 – 250. Variation of Q over time is not clear (Figure 6.8b) probably because the duration is too short (1 to 2 days). Given a longer duration, we can track the changes in attenuation over time.

Figure 6.9 shows the profile of Q compared with density, V_p , and V_s from well logs. Less consolidated sediments tend to have lower values of Q , density, and velocity. Hence, the increase in density, V_p , and V_s between 1.5 – 2.0 km is consistent with the higher Q . The cause of the lower apparent Q below 2.0 km is not certain. We note that since the events are not directly in line with the cable, channels near the source (near the bottom of the cable) might have the source term not properly canceled out, which can add to uncertainty in the Q measurements. Another source of uncertainty is the instrument response removal, which depends on the apparent velocity and hence the picking accuracy. Picking near the source might be compromised by the arrival of sequential phases.

Figure 6.10 shows the comparison between Q , density, V_p , and V_s . For density above 2.3 g/cm³, $V_p > 3$ km/s, and $V_s > 1.2$ km/s, Q generally varies between 30 – 600 with an average of around 130. Below these thresholds, Q decreases drastically to a range between 20 and 50.

6.5 Source parameter analysis

We first consider modeling source parameters using a single spectra approach that models the spectra of individual events. Then, we try finding collocated event pairs for another spectral ratio approach.

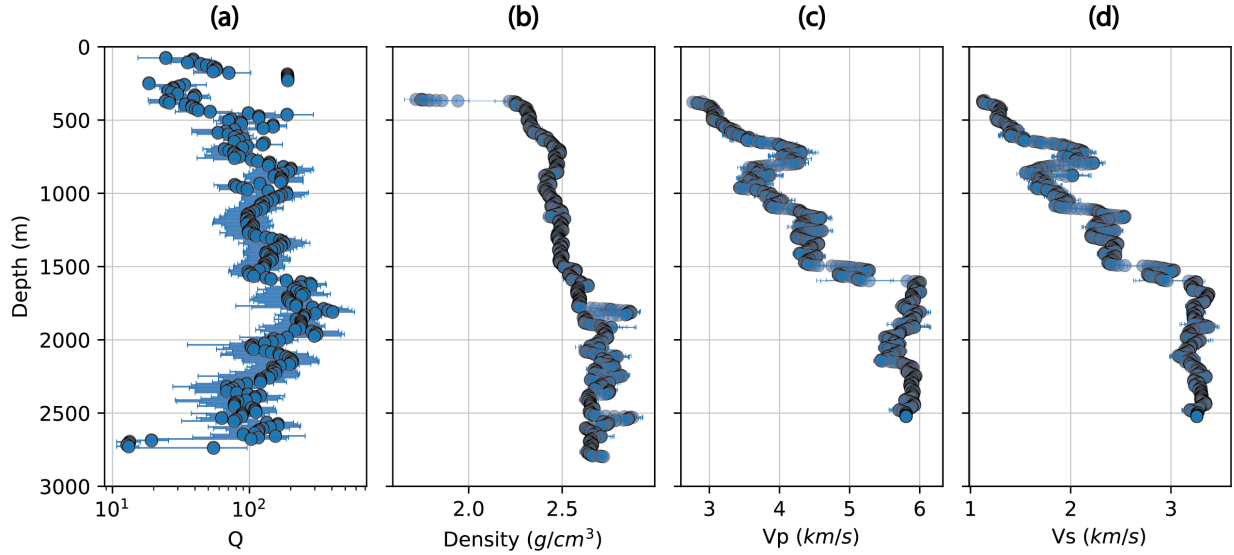


Figure 6.9: Along-depth profiles of (a) Quality factor (Q), (b) density, (c) P-wave velocity (V_p), and (d) S-wave velocity (V_s). The Q values are estimated using deconvolved P-wave spectra. Density, V_p , and V_s are obtained from well logs (gamma ray and sonic logs). Each dot is the median of measurements within 20 m. The error bars indicate median absolute deviations.

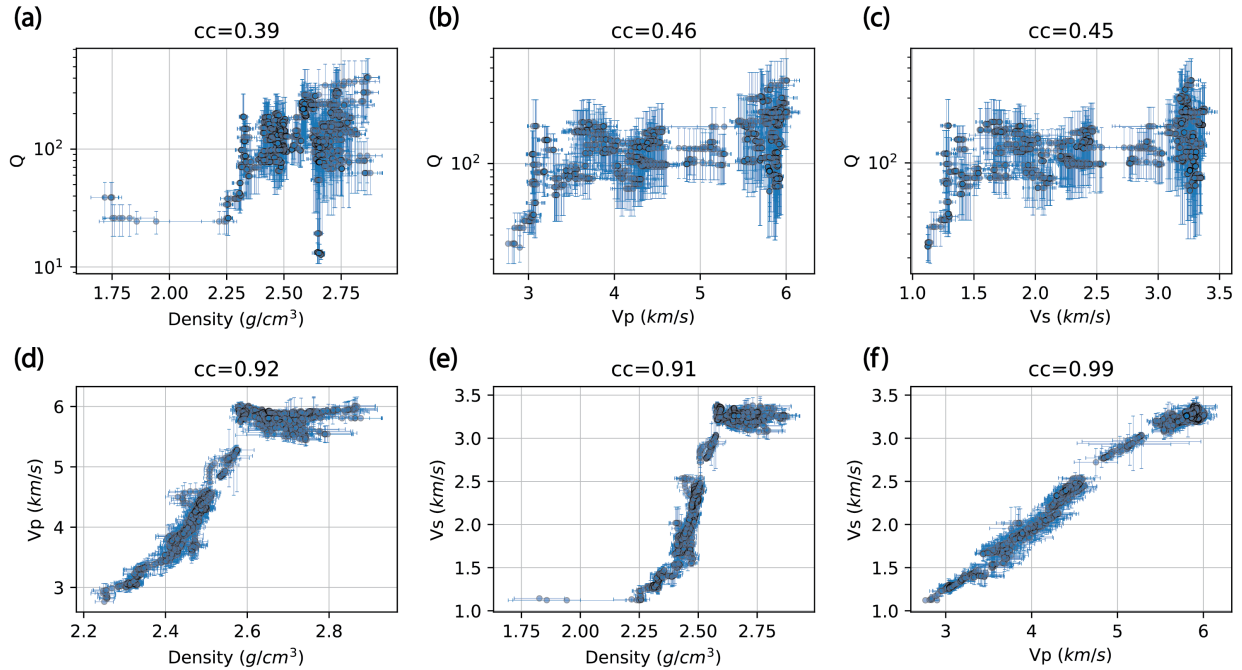


Figure 6.10: Comparison between Quality factor (Q), density, P-wave velocity (V_p), and S-wave velocity (V_s). (a) Q vs. density, (b) Q vs. V_p , (c) Q vs. V_s , (d) V_p vs. density, (e) V_s vs. density, (f) V_p vs. V_s . The Q values are estimated using deconvolved P-wave spectra. Density, V_p , and V_s are obtained from well logs (gamma ray and sonic logs). Each dot is the median of measurements within 20 m. The error bars indicate median absolute deviations. All non-zero cross-correlation coefficients (cc) shown here have a p-value < 5%.

6.5.1 Single spectra approach

Theory

The far-field displacement source spectra (Ω) can be modeled as (Brune, 1970; Boatwright, 1978, 1980):

$$\Omega(f) = \frac{\Omega_0 e^{-(\pi f t/Q)}}{[1 + (f/f_c)^{\gamma n}]^{1/\gamma}}, \quad (6.8)$$

where f is frequency, Ω_0 is the amplitude at the low-frequency asymptote, f_c is the corner frequency, and n is the high-frequency fall-off rate.

The observed far-field displacement spectra (Ω_R) include an exponential attenuation term:

$$\Omega_R(f) = \Omega e^{-\pi f \kappa}, \quad (6.9)$$

in which κ is the high-frequency attenuation parameter. In this study, we assume the attenuation consists of a path and a site term (Chang et al., 2025); that is:

$$\kappa = \kappa_{path} + \kappa_{site}, \quad (6.10)$$

$$\approx \frac{t_{path}}{Q_{path}} + \frac{t_{site}}{Q_{site}}, \quad (6.11)$$

in which the path and site-dependent attenuation term have their associated travel times (t_{path} and t_{site}) and quality factors (Q_{path} and Q_{site}).

The seismic moment is (Madariaga, 1976)

$$M_0 = \frac{4\pi\rho c^3 R \Omega_0}{U_{\phi\theta}}, \quad (6.12)$$

in which ρ is density (assumed to be $2,790 \text{ kg/m}^3$), c is the P-wave velocity at the hypocenter, R is the hypocentral distance, and $U_{\phi\theta}$ is the mean radiation pattern coefficient for P waves (0.52 based on Madariaga, 1976).

The moment magnitude is (Hanks & Kanamori, 1979)

$$M_w = (\log_{10} M_0 - 9.05)/1.5. \quad (6.13)$$

The source radius (r) can be estimated from the corner frequency (Brune, 1970; Madariaga, 1976):

$$r = k\beta/f_c, \quad (6.14)$$

in which k is a constant that depends on the theoretical rupture model and β is the S-wave velocity at the hypocenter. We assume $k = 0.38$ for P waves when $n = 2$ and a rupture velocity of 0.9β (Kaneko & Shearer, 2015).

The static stress drop for a circular crack can be expressed by the moment and the source radius (Eshelby, 1957; Madariaga, 1976):

$$\Delta\sigma = \frac{7}{16} \frac{M_0}{r^3}. \quad (6.15)$$

Data processing

We focus on 1155 events that occur between February 27 – March 6 with good quality arrival times (picked using a kurtosis picker). We window the P waves at -0.05 – 0.05 s around the P arrival time. Figure 6.11a shows the amplitude spectra of the raw data, which is proportional to acceleration.

We convert the raw data to particle displacement using Equations 6.3 and 6.6 (Figure 6.11b). We remove the gauge length response by dividing the spectra by the response estimated using Equation 6.2 (Figure 6.11c). The apparent velocities in Equations 6.6 and 6.2 for each channel are estimated by dividing the channel separations by the picked arrival times. To avoid amplifying noise, we put a high-frequency cutoff on the response spectra to mute points with an estimated response lower than 0.4. Channels with a cutoff frequency of less than 200 Hz are discarded. We resample the spectra to a constant interval in the frequency domain and discard spectral points with $\text{SNR} < 3$. We only use channel numbers from 820 to 1100 where the SNR is consistent among events and the available frequency band generally reaches 400 Hz. To enhance SNR, we stack channels every 20 m (10 channels in one stack).

We use a least-square approach (Newville et al., 2016) to fit the spectral model Ω_R (Equation 6.9) to the stacked displacement spectra (Figure 6.12). In the model, we use the median Q_{site} estimated in the attenuation analysis for each stacked spectrum and assume t_{site} is 10% of the total travel time. The 10% is a rough empirical value. We just need a t_{site} that is much smaller than t_{path} so that κ_{site} is mainly site dependent (Chang et al., 2025). We fix $n = 2$ to prevent parameter trade-offs (Kaneko & Shearer, 2015; Chang et al., 2025) and use the Boatwright model ($\gamma = 2$; Boatwright, 1978). The dependent parameters are f_c and Ω_0 . We try both fixing $Q_{path} = 600$ and allowing Q_{path} to be flexible.

After obtaining f_c and Ω_0 , we estimate the seismic moment (Equation 6.12), moment magnitude (Equation 6.13), and the source radius (Equation 6.14).

Results

Figure 6.13 shows the single spectra modeling results for the events. The lowest magnitude that we can resolve the corner frequency is approximately -0.5, restricted by the upper bandwidth limit. The majority of the events have stress drops ($\Delta\sigma$) generally following a constant relation in between $M_w = -0.5 – 1.7$ with scattering between 1 and 20 MPa (Figure 6.13a). If allowing Q_{path} to vary, we get $Q_{path} = 10 – 3000$ (Figure 6.13b). However, we suspect the correlation between Q_{path} and $\Delta\sigma$ in Figure 6.13b may be due to parameter trade-offs in the fitting process. Hence, we choose to stick to a fixed Q_{path} for the rest of the analysis to simplify the problem. The stress drops assuming a fixed Q_{path} do not have a large correlation with distance, source depth, or source radius (Figure 6.14b,c,d). The slightly higher correlation between $\Delta\sigma$ and M_w (Figure 6.14a) may be due to the upper bandwidth limit.

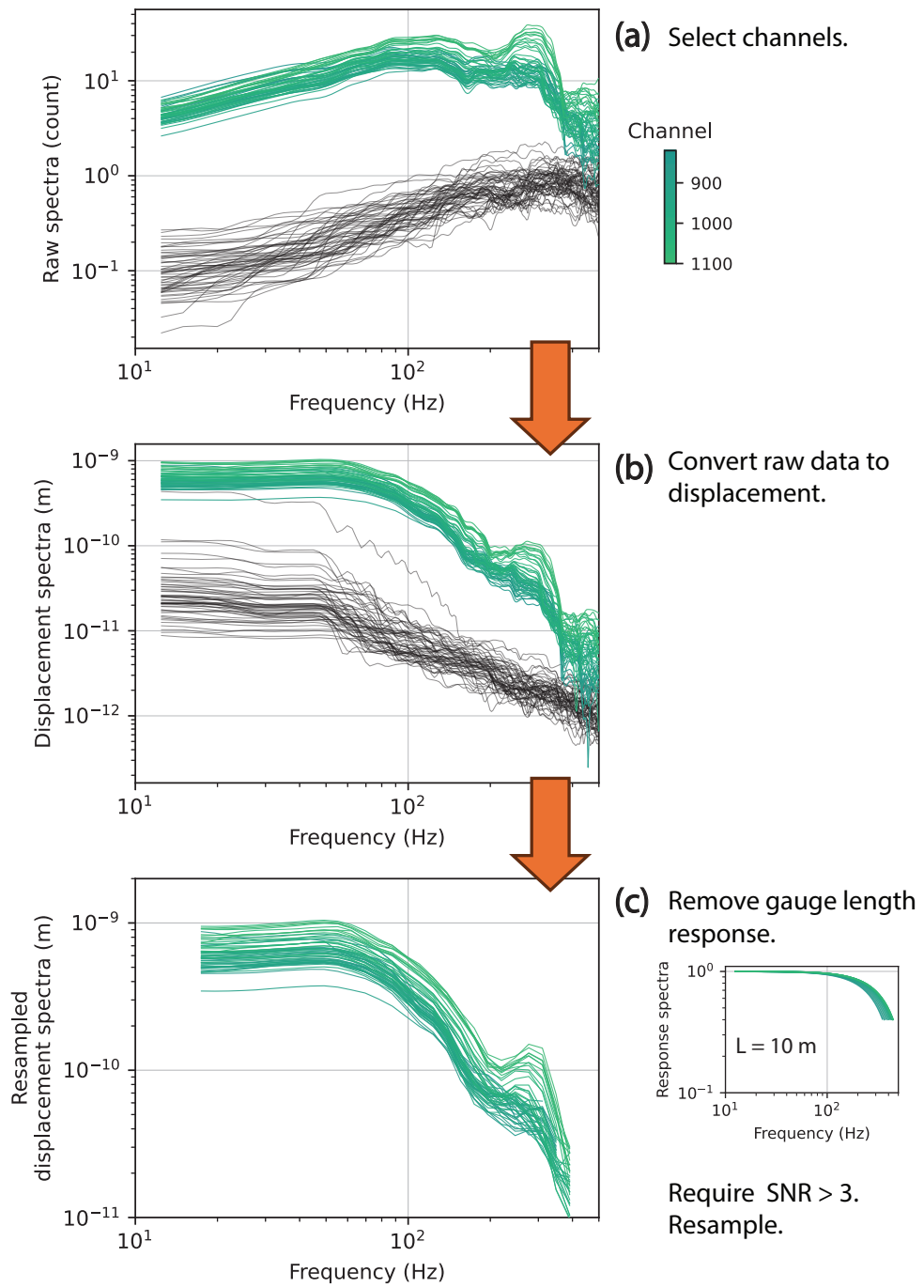


Figure 6.11: Data treatments before the single spectra fitting approach for an event. Color curves are P-wave spectra and black curves are noise spectra. **(a)** The raw DAS data (proportional to strain rate). We choose to process data from channels 820 – 1100 which have stable data quality. **(b)** The converted displacement spectra. **(c)** The spectra after (1) removing the gauge length (L) responses (small inset in **c**), (2) point-wise quality controls that require signal-to-noise ratios > 3 , and (3) resampling to have a constant interval in the frequency domain.

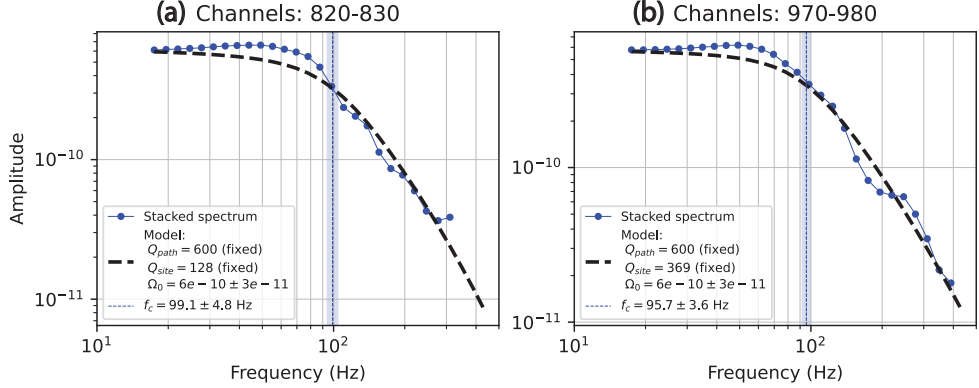


Figure 6.12: Single spectra fitting examples for an event. The blue dots and curves are the stacked displacement spectra (stack of the 10 closest channels). The black dashed curves are the model. The vertical dashed lines indicate the corner frequency (f_c). Both the path- and site-dependent attenuation (Q_{path} and Q_{site}) are fixed in these examples. We also try using a flexible Q_{path} (see Figure 6.13).

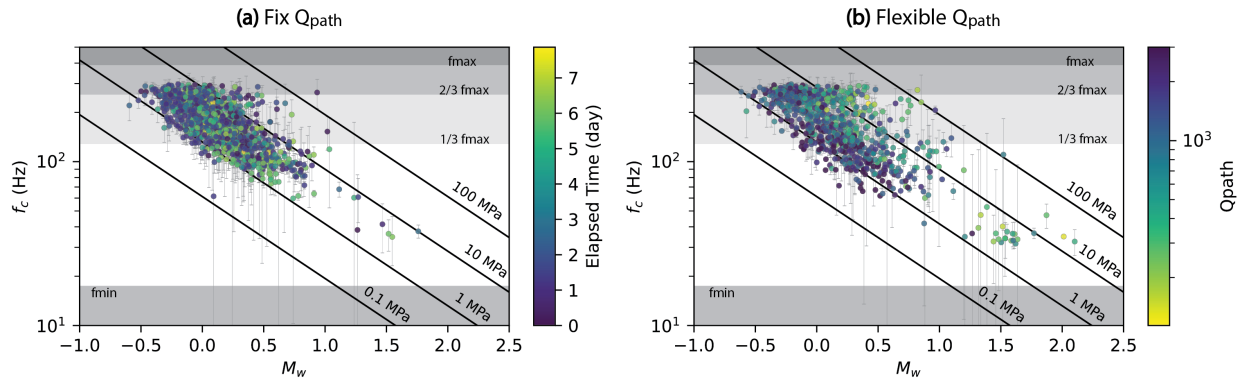


Figure 6.13: Corner frequency (f_c), moment magnitude (M_w), and apparent stress drop ($\Delta\sigma$) are estimated using the single spectra approach. The solid lines indicate constant stress drops of 0.1, 1, 10, and 100 MPa. We try (a) fixing path-dependent attenuation (Q_{path}) at 600, and (b) letting Q_{path} be flexible as a dependent variable. Each dot is the median value of all available measurements for an event on the selected cable segment in well 1OB. The error bars indicate the standard deviation. f_{max} and f_{min} are the median maximum and minimum available frequency bandwidth, respectively, defined by the signal-to-noise ratio.

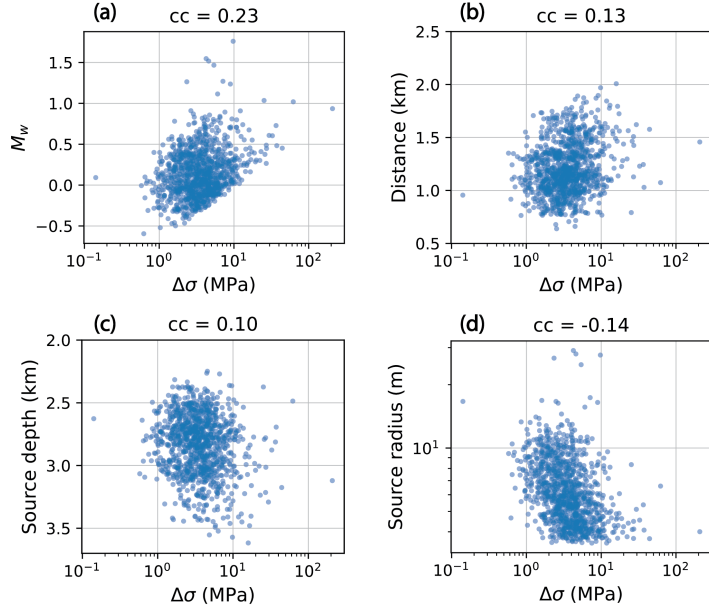


Figure 6.14: Correlations between apparent stress drop ($\Delta\sigma$) and (a) estimated moment magnitude (M_w), (b) hypocentral distance, (c) source depth, and (d) source radius. All non-zero cross-correlation coefficients (cc) shown are significant (p -values $< 5\%$).

Most events have source radius between 3 – 20 m (Figure 6.15a) and stress drops between 1 – 20 MPa (Figure 6.15b). The moment magnitudes estimated by DAS positively correlate with the moment magnitudes in the catalog (Figure 6.16). The quality of the catalog magnitude is uncertain and there are likely biases (personal communication with N. Nakata). Hence, we do not attempt to interpret the difference between the DAS and the catalog magnitudes; instead, we highlight the positive correlation between the DAS and the catalog magnitudes, which suggests the potential of using DAS for magnitude estimation for small earthquakes.

Figure 6.17 shows the spatial distribution of stress drops. Some larger clusters close to the injection wells (F-3I and F-2P) appear to have events with lower stress drops. The average stress drops increase with distance to the injection point (Figure 6.18). We bin the $\Delta\sigma$ measurements into 10 distance bins (the red curve) and conduct a one-way ANOVA

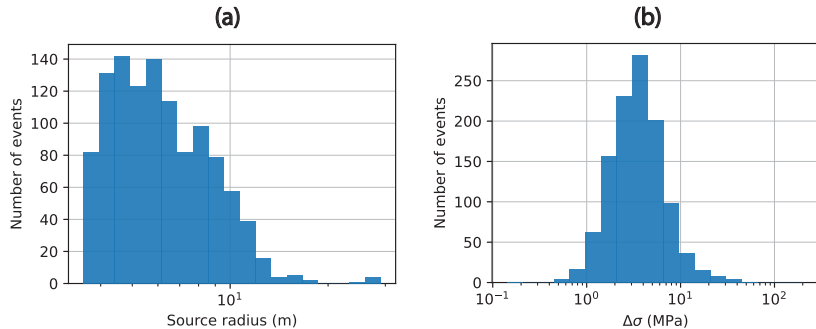


Figure 6.15: (a) Source radius and (b) stress drop distributions using the single spectra approach.

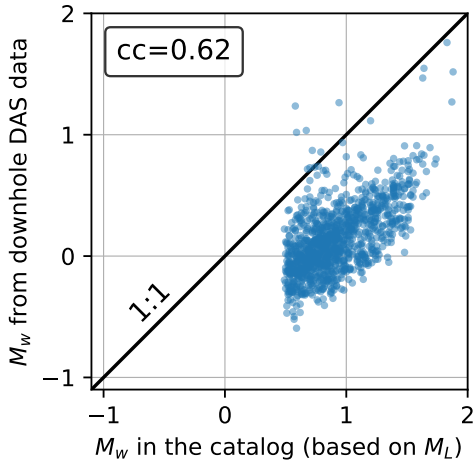


Figure 6.16: Moment magnitudes (M_w) estimated by downhole DAS data using single spectra fitting vs. M_w in the catalog. The catalog used surface geophones to estimate local magnitudes (M_L) and then converted them to M_w using an empirical relation. The M_w estimated by DAS data positively correlates with catalog magnitudes. The catalog magnitudes might be overestimated by 1 order of magnitude.

test (Heiman, 2001), which uses the F value to examine the significance. The test suggests statistical significance (an F value = 3.7 with a p-value < 5%) for increasing $\Delta\sigma$ with increasing distance from the injection. Events within 0.5 km have $\Delta\sigma \sim 3$ MPa and increase to 4 – 6 MPa for events 1 km away.

6.5.2 Spectral ratio approach

Theory

Another source characterization method that deals with the propagation effect is the spectral ratio method (e.g., Hartzell, 1978; Hough, 1997). The spectral ratio method does not require assuming attenuation. To perform the spectral ratio method, we need to find a collocated event pair with a similar focal mechanism. The large event is the target event and the small event is the Empirical Green's Function (EGF). The event pair shares the same path, site, and instrument responses. Hence, dividing their far-field spectra can isolate the source terms.

The spectral ratio is:

$$\Omega_r(f) = \Omega_{0r} \left[\frac{1 + (f/f_{c2})^{\gamma n}}{1 + (f/f_{c1})^{\gamma n}} \right]^{1/\gamma}, \quad (6.16)$$

which is the far-field spectra (e.g., Equation 6.8) of the target event divided by that of the EGF event. Ω_{0r} is the relative low-frequency amplitude of the event pair. f_{c1} and f_{c2} are the corner frequencies of the target and the EGF events, respectively. Similar to Section 6.5.1, we assume $\gamma = 2$ and $n = 2$.

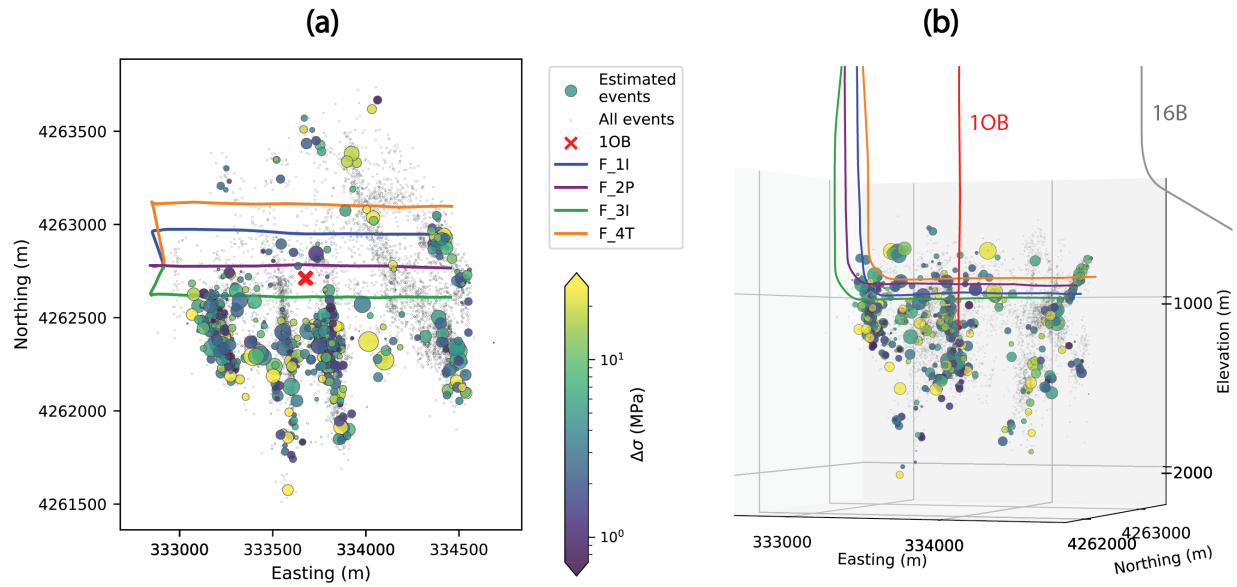


Figure 6.17: Event stress drop (a) 2D and (b) 3D maps using the single spectra approach. Events with eligible stress drop estimates are shown in colored circles with their sizes proportional to the moment magnitude results. The small black dots represent other events. See legend for the well names.

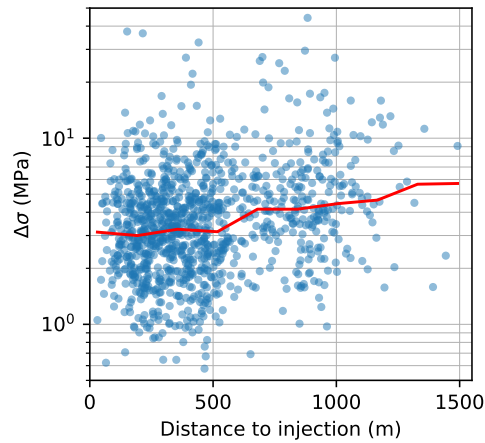


Figure 6.18: Stress drop ($\Delta\sigma$) vs. distances to the injection. The red curve shows the median values in 10 distance bins. An F test (Heiman, 2001) suggests the statistical significance of increasing $\Delta\sigma$ with increasing distance to the injection.

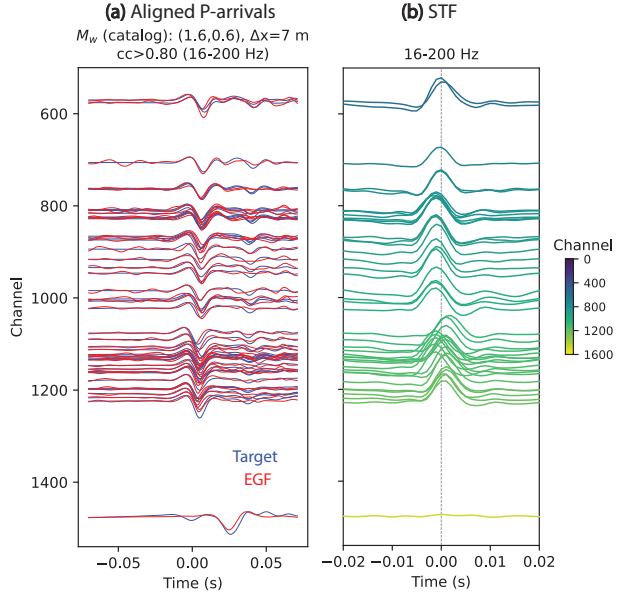


Figure 6.19: (a) Aligned P-arrival waveforms of a target (blue) and EGF (red) event pair and (b) the Source Time Function (STF) calculated by deconvolving the target by the EGF. The time window used for calculating the STF is $-0.07 - 0.07$ s to the P-arrival. The waveforms are normalized by the maximum amplitude.

Data processing

We first find event pairs that are < 0.1 km (uncertainty of the location) from each other. The low-frequency amplitude ratio between the target and EGF events needs to be large enough to allow proper determination of f_{c1} . We require the amplitude ratio to be > 2 following Abercrombie (2014) and Abercrombie (2015) and the catalog magnitude difference to be > 0.5 .

After aligning the P arrivals in time, we cut the waveforms at $-0.07 - 0.07$ s relative to the P arrival time. We require $cc > 0.8$ for the waveforms filtered between 1 and 50 Hz (Abercrombie, 2015; Pennington et al., 2022). Note that the bandpass filter is only for getting the bandwidth below general corner frequencies in this step and we do not filter the waveforms used in the later spectral fitting. We discard spectral points with $\text{SNR} < 3$. Then, we divide the target event spectra by the EGF spectra. Most of the spectral ratios that pass the quality controls are between channel 600 and 1300.

Figure 6.19 shows an event with aligned P arrivals along the cable that passes the quality control and the Source Time Functions (STFs). The STF is the spectral ratio in the time domain, and it characterizes the temporal evolution of the rupture pulse. With densely spaced channels on the cable, we can characterize the spatial evolution of the pulse.

We resample the spectral ratios to have equal frequency intervals in the logarithmic space. Then, we stack and fit the stacked spectral ratios with Equation 6.16 (Figure 6.20). The dependent variables are Ω_{0r} , f_{c1} , and f_{c2} . To avoid trade-offs between f_{c1} and f_{c2} (Shearer

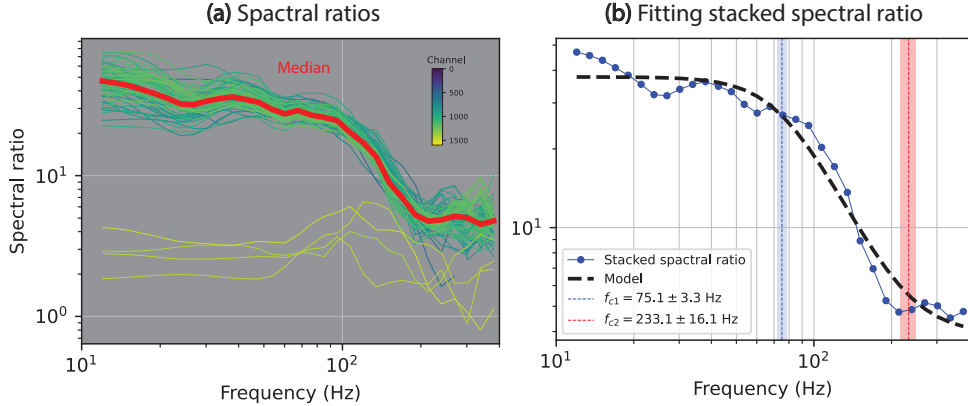


Figure 6.20: (a) Spectral ratios of an event pair and (b) modeling the stacked spectral ratio. In (a), the red curve is the median of the spectral ratios (the stacked ratio). In (b), the black dashed curve is the best-fitted model to the stacked ratio (blue dots and curve). The corner frequencies of the target event and the EGF are f_{c1} and f_{c2} , respectively.

et al., 2019), we also try fixing f_{c2} , in which we fix f_{c2} at an event-dependent value calculated assuming a constant stress drop of 3.4 MPa (median of the single spectra results) and the seismic moments estimated in the single spectra approach. For the final results, we require $f_{c1} < 2/3f_{c2}$, an uncertainty of f_{c1} (standard deviation in the fitting divided by the results) < 10%, and a mean absolute residual smaller than an empirical threshold. We use the seismic moments estimated in the single spectra approach to calculate stress drops (Equation 6.15).

Results

Figure 6.21 shows the fitting results using the spectral ratio approach. The trend of $\Delta\sigma$ along M_w is not clear due to the limited magnitude range and scatters in $\Delta\sigma$. The error bars in Figure 6.21 only indicate the standard deviation in the least-square fitting and likely underestimate the large uncertainties that come from EGF assumptions (e.g., Abercrombie, 2015). If allowing f_{c2} to vary, the f_{c1} and $\Delta\sigma$ in Figure 6.21a likely have trade-offs with f_{c2} . Fixing f_{c2} gives a range of $\Delta\sigma$ between 1 and 15 MPa.

Figure 6.22 compares the corner frequency estimated using spectral ratio and single spectra approaches. If making f_{c2} a dependent variable (Figure 6.22a), f_{c1} appears to increase with f_{c2} , with leads to disagreement with f_c determined using the single spectra method. Fixing f_{c2} in the spectra ratio approach results in better agreements between the two approaches, although the correlation is not significant probably due to a lack of data points.

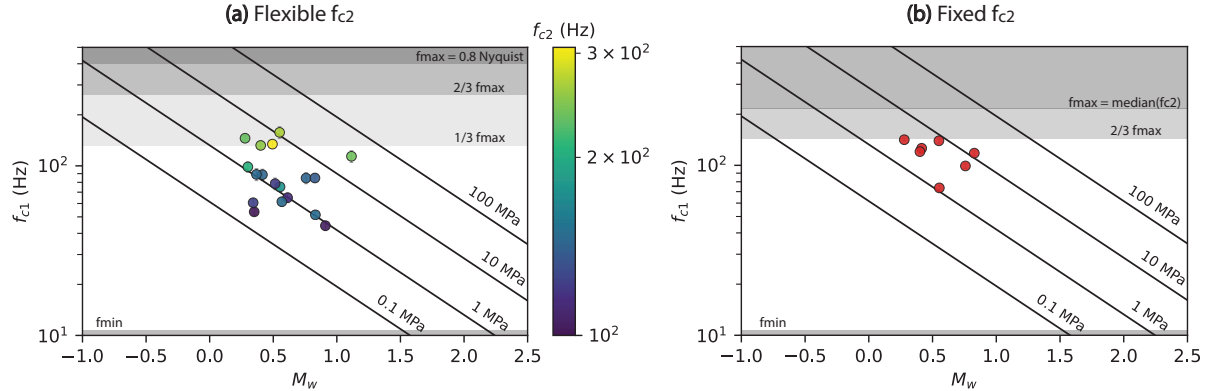


Figure 6.21: Corner frequency (f_{c1}) and apparent stress drop ($\Delta\sigma$) of target events are estimated using the spectral ratio approach. **(a)** Allowing f_{c2} to vary and **(b)** fixing f_{c2} at an event-dependent value assuming a constant stress drop of 3.4 MPa and a seismic moment based on the single spectral fitting results. The moment magnitudes (M_w) are taken from the single spectra approach. The solid lines indicate constant stress drops of 0.1, 1, 10, and 100 MPa. Each dot represents the result of an event. The error bars indicate the standard deviation of f_{c1} in the least-square fitting approach (likely underestimating the uncertainties from other sources).

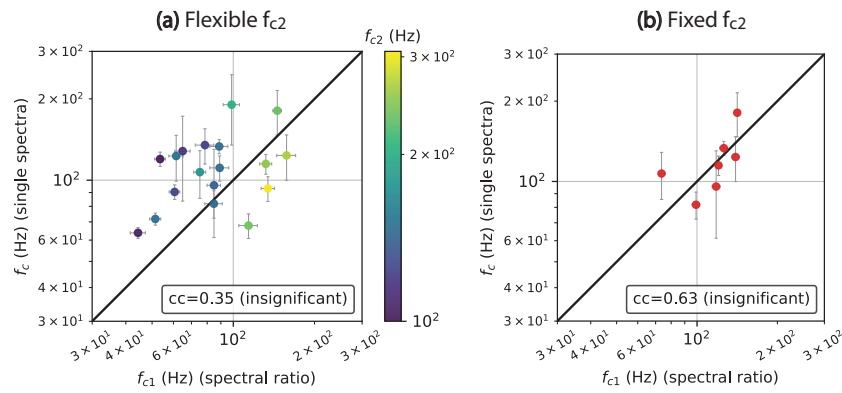


Figure 6.22: Comparing corner frequency estimated using single spectra (f_c) and **(b)** spectral ratio (f_{c1}) approaches. **(a)** Allowing f_{c2} to vary, and **(b)** fixing f_{c2} in the spectral ratio approach. The error bars indicate the standard deviation of the least-square fitting approach. The cross-correlation coefficients (cc) are not significant (p -values $> 5\%$) likely because of the small number of data points.

6.6 Discussions

Attenuation resolved by DAS

The attenuation resolved by DAS generally decreases with depth in the sediment column. Comparing with well logs, the sudden drop of Q at around 0.5 km depth corresponds to density $< 2.3 \text{ g/cm}^3$, $V_p < 3 \text{ km/s}$, and $V_s < 1.2 \text{ km/s}$. These thresholds can be useful for estimating attention at other sites since in-situ densely spaced attenuation measurements are rare but we can often obtain seismic velocity profiles.

Q still varies across a wide range (30 – 600) at higher density, V_p , and V_s . Some of the variability of Q at deeper depths might be caused by the source term of the events not being properly canceled out, which can be analyzed by observing more events. Another uncertainty comes from the gauge length response removal, which depends on the apparent velocity (Section 6.3.1), and hence depends on picking accuracy. An improved arrival picker can reduce the potential of mistakenly picking a later arriving phase and thus avoid getting a biased instrument response.

A workflow for modeling source parameters

Modeling source parameters using single spectra has the advantage of having a lot more available measurements, while the cons are the need to assume the wave propagation effects and instrument responses. The spectral ratio approach has the advantage of avoiding making wave propagation and response assumptions, which can be favorable, especially for DAS. However, the assumption of EGF can bring in large uncertainties as well ([Abercrombie, 2015](#)).

We provide a workflow for using downhole DAS for characterizing source parameters. First, we investigate the instrument response; second, we characterize the attenuation; third, we model single spectra to get source parameters using the attenuation we obtain; fourth, we proceed with the spectral ratio approach where we constrain the EGF using results from single spectra fitting. This workflow allows us to take advantage of the different methods and compare them in the end.

Stress drop interpretation

The stress drops generally follow a constant trend between 1 and 10 MPa for events M_w -0.5 – 1.7. The increasing stress drop with distance from the injection point agrees with previous observations in the Bessel geothermal field ([Goertz-Allmann et al., 2011](#)). This phenomenon can be explained by larger stress perturbation near the injection allowing faults that are not critically stressed in the background stress field to fail, thus allowing events triggered under a lower differential stress ([Goertz-Allmann & Wiemer, 2013](#)).

To reduce trade-offs between parameters, we choose to reduce the number of dependent

variables in the fitting process, which involves some simplifications (e.g., a simplified attenuation model). A more detailed examination of the validity of the assumptions (e.g., using a more sophisticated attenuation model) can improve the accuracy of the results and potentially reveal meaningful trends between stress drops and other parameters.

Other future improvements

In this study, we use a simple automatic picker to pick arrivals. We discard many events that the picker cannot reliably pick in the analysis. The future plan is to use a picker with better performance (e.g., PhaseNet DAS; [Zhu et al., 2023](#)) so that we can include more events. This will allow us to better characterize the spatial distribution of stress drops and potentially give us more available collocated event pairs for the spectral ratio analysis. Another future plan is to include cables in other horizontal and deviated wells (e.g., well 16B in Figure 6.1). Including DAS measurements in different orientations will allow us to resolve the focal mechanism and also invert the source slip pattern.

6.7 Conclusions

We develop a workflow for characterizing attenuation and earthquake source parameters using downhole Distributed Acoustic Sensing (DAS). In the workflow, we first consider the instrument response of DAS, resolve the attenuation, and then analyze the source parameters.

We explore the unit conversion and the gauge length response, which involve assumptions such as plane waves and medium velocity. We use an along-depth deconvolution to resolve the attenuation. The attenuation increases drastically at the near-surface (< 0.5 km) when density drops below 2.3 g/cm³, $V_p < 3$ km/s, and $V_s < 1.2$ km/s.

We model source parameters using two different approaches: the single spectra approach and the spectral ratio approach. We successfully characterize corner frequency, moment magnitude, and stress drop for \sim 1000 events during one-week stimulation at the Cape Modern geothermal field. The moment magnitude is between -0.5 – 1.7. The majority of stress drops are between 1 – 10 MPa and generally follow a constant trend of stress drop across magnitudes. The source radius derived from the corner frequency is 3 – 20 m. This study demonstrates the potential of using downhole DAS for characterizing shallow structures and microearthquakes ($M < 2$).

References

- Abercrombie, R. E. (2014). Stress drops of repeating earthquakes on the San Andreas fault at parkfield. *Geophysical Research Letters*, 41(24), 8784–8791.

- Abercrombie, R. E. (2015). Investigating uncertainties in empirical Green's function analysis of earthquake source parameters. *J. Geophys. Res.*, 120(6), 4263–4277.
- Anderson, J. G. & Hough, S. E. (1984). A model for the shape of the Fourier amplitude spectrum of acceleration at high frequencies. *Bulletin of the Seismological Society of America*, 74(5), 1969–1993.
- Bakku, S. K. (2015). *Fracture characterization from seismic measurements in a borehole*. PhD thesis, Massachusetts Institute of Technology.
- Beyreuther, M., Barsch, R., Krischer, L., Megies, T., Behr, Y., & Wassermann, J. (2010). ObsPy: A Python toolbox for seismology. *Seismol. Res. Lett.*, 81(3), 530–533.
- Boatwright, J. (1978). Detailed spectral analysis of two small new york state earthquakes. *Bulletin of the Seismological Society of America*, 68(4), 1117–1131.
- Boatwright, J. (1980). A spectral theory for circular seismic sources; simple estimates of source dimension, dynamic stress drop, and radiated seismic energy. *Bulletin of the Seismological Society of America*, 70(1), 1–27.
- Brune, J. N. (1970). Tectonic stress and the spectra of seismic shear waves from earthquakes. *J. Geophys. Res.*, 75(26), 4997–5009.
- Chang, H., Abercrombie, R. E., & Nakata, N. (2025). Importance of considering near-surface attenuation in earthquake source parameter estimation: Insights from kappa at a dense array in oklahoma. *Bulletin of the Seismological Society of America*.
- Chen, X. (2023). Source parameter analysis using distributed acoustic sensing—an example with the PoroTomo array. *Geophysical Journal International*, 233(3), 2208–2214.
- Eshelby, J. D. (1957). The determination of the elastic field of an ellipsoidal inclusion, and related problems. *Proceedings of the Royal Society of London — Series A: Mathematical and Physical Sciences*, 241(1226), 376–396.
- Goertz-Allmann, B. P., Goertz, A., & Wiemer, S. (2011). Stress drop variations of induced earthquakes at the basel geothermal site. *Geophysical Research Letters*, 38(9).
- Goertz-Allmann, B. P. & Wiemer, S. (2013). Geomechanical modeling of induced seismicity source parameters and implications for seismic hazard assessment. *Geophysics*, 78(1), KS25–KS39.
- Hanks, T. C. & Kanamori, H. (1979). A moment magnitude scale. *J. Geophys. Res.*, 84(B5), 2348–2350.
- Hartog, A. (2017). *An Introduction to Distributed Optical Fibre Sensors*. Boca Raton, FL, USA: CRC Press.
- Hartzell, S. H. (1978). Earthquake aftershocks as Green's functions. *Geophys. Res. Lett.*, 5(1), 1–4.
- Heiman, G. W. (2001). *Understanding research methods and statistics: An integrated introduction for psychology*. Houghton, Mifflin and Company.
- Hough, S. (1997). Empirical Green's function analysis: Taking the next step. *J. Geophys. Res.*, 102(B3), 5369–5384.
- Kaneko, Y. & Shearer, P. (2015). Variability of seismic source spectra, estimated stress drop, and radiated energy, derived from cohesive-zone models of symmetrical and asymmetrical circular and elliptical ruptures. *Journal of Geophysical Research: Solid Earth*, 120(2), 1053–1079.
- Lior, I. (2024). Accurate magnitude and stress drop using the spectral ratios method applied to distributed acoustic sensing. *Geophysical Research Letters*, 51(1), e2023GL105153.

- Madariaga, R. (1976). Dynamics of an expanding circular fault. *Bull. Seismol. Soc. Am.*, 66(3), 639–666.
- Nakata, N., Chang, H., Wu, S.-M., Bi, Z., Chen, L.-W., Soom, F., Gao, H., Titov, A., & Dadi, S. (2025). Fracture characterization revealed by microseismicity at cape modern geothermal field, utah. In *Proc. of the 50th Workshop on Geothermal Reservoir Engineering*.
- Nakata, N., Wu, S.-M., Hopp, C., Robertson, M., & Dadi, S. (2024). Microseismicity observation and characterization at Cape Modern and Utah FORGE. In *Proc. of the 49th Workshop on Geothermal Reservoir Engineering*.
- Newville, M., Stensitzki, T., Allen, D. B., Rawlik, M., Ingargiola, A., & Nelson, A. (2016). LMFIT: Non-linear least-square minimization and curve-fitting for Python. *Astrophysics Source Code Library*, (pp. ascl-1606).
- Pennington, C. N., Chang, H., Rubinstein, J. L., Abercrombie, R. E., Nakata, N., Uchide, T., & Cochran, E. S. (2022). Quantifying the sensitivity of microearthquake slip inversions to station distribution using a dense nodal array. *Bull. Seismol. Soc. Am.*, 112(3), 1252–1270.
- Prieto, G. A. (2022). The multitaper spectrum analysis package in Python. *Seismological Society of America*, 93(3), 1922–1929.
- Shearer, P. M., Abercrombie, R. E., Trugman, D. T., & Wang, W. (2019). Comparing EGF methods for estimating corner frequency and stress drop from P wave spectra. *Journal of Geophysical Research: Solid Earth*, 124(4), 3966–3986.
- Wang, H. F., Zeng, X., Miller, D. E., Fratta, D., Feigl, K. L., Thurber, C. H., & Mellors, R. J. (2018). Ground motion response to an M_L 4.3 earthquake using co-located distributed acoustic sensing and seismometer arrays. *Geophysical Journal International*, 213(3), 2020–2036.
- Zhan, Z. (2020). Distributed acoustic sensing turns fiber-optic cables into sensitive seismic antennas. *Seismological Research Letters*, 91(1), 1–15.
- Zhu, W., Biondi, E., Li, J., Yin, J., Ross, Z. E., & Zhan, Z. (2023). Seismic arrival-time picking on distributed acoustic sensing data using semi-supervised learning. *Nature Communications*, 14(1), 8192.